

Kernelized Back-Projection Networks for Blind Super Resolution

Tomoki Yoshida[†], Yuki Kondo[†], Takahiro Maeda, Kazutoshi Akita, and Norimichi Ukita *Member, IEEE*

Abstract—Since non-blind Super Resolution (SR) fails to super-resolve Low-Resolution (LR) images degraded arbitrarily, SR with the degradation model is required. However, this paper reveals that non-blind SR trained simply with various blur kernels exhibits comparable performance as those with the degradation model for blind SR. This result motivates us to revisit high-performance non-blind SR and extend it to blind SR with blur kernels. This paper proposes two SR networks by integrating kernel estimation and SR branches in an iterative end-to-end manner. In the first model, which is called the Kernel Conditioned Back-Projection Network (KCBPN), the low-dimensional kernel representations are estimated for conditioning the SR branch. In our second model, the Kernelized Back-Projection Network (KBPN), a raw kernel is estimated and employed for modeling the image degradation. The estimated kernel is employed not only for back-propagating a residual from its ground-truth but also for forward-propagating the residual to iterative stages. This forward-propagation encourages these stages to learn a variety of different features in different stages by focusing on pixels with large residuals in each stage. Experimental results validate the effectiveness of our proposed networks for kernel estimation and SR. We will release the code for this work*.

Index Terms—Blind SR, Blur Kernel, Iterative stages

I. INTRODUCTION

Image Super-Resolution (SR) [1] reconstructs a High-Resolution (HR) image, I^{HR} , from its Low-Resolution (LR) image, I^{LR} . We model the image degradation process from HR to LR as follows:

$$I^{LR} = (I^{HR} * K) \downarrow_s, \quad (1)$$

where K , \downarrow , and s denote a blur kernel, a downsampling process, and a scaling factor, respectively.

While early SR methods assume only a single degradation with no blur kernel, recent methods model the blur kernel in Eq. (1) [2]–[4], [6]–[15]. While the superiority of the kernel SR methods is demonstrated in comparison with those with no kernel, these non-kernel SR methods are trained with images degraded by only a single degradation process (e.g., bicubic downsampling with no blur kernel in Eq. (1)) in the literature. To validate the effectiveness of the kernel SR, it is worth exploring to revisit whether or not the non-kernel SR methods can be improved by being trained with variedly-degraded images. Based on this revisit, this paper proposes two kernelized SR networks by integrating the advantages of kernel estimation and high-performance non-blind SR networks. Our novel contributions are summarized as follows:

All authors are with Toyota Technological Institute, Nagoya, 468-8511 Japan (e-mail: ukita@toyota-ti.ac.jp).

[†] The first two authors contributed equally to this work.

* : This code will be released in <https://github.com/Yuki-11/KBPN>.

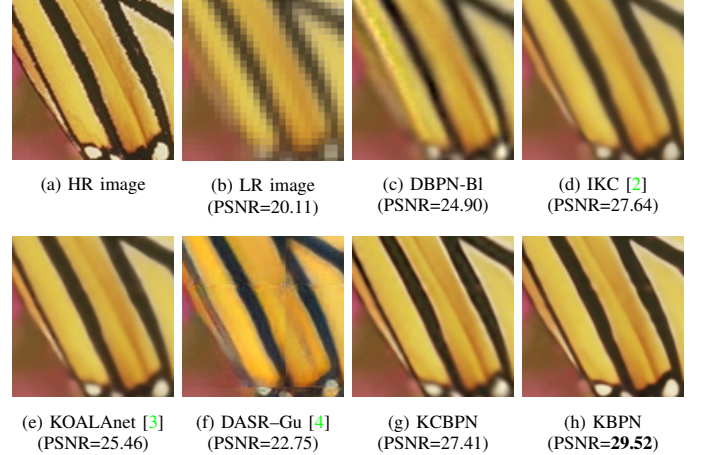


Fig. 1: Visual comparison of SR methods for an unknown kernel. The LR image **b** is generated from its HR image **a** by Eq. (1) with the anisotropic Gaussian blur kernel ($\sigma_x/\sigma_y = 2.6/4.0$). While the non-blind SR model trained with various blurs **c** is comparable with blind SR **d e**, our method **h** reconstructs sharper boundaries.

- We empirically found that non-kernel SR can be improved by being trained with variedly-degraded images.
- Based on the above finding, two SR networks (Fig. 1 **g** and **h** and Fig. 2 **c** and **d**) are proposed by iteratively integrating kernel estimation and SR feature enhancement. While the first network conditions SR features by a low-dimensional kernel representation, a raw blur kernel is employed with Eq. (1) for our proposed SR feature enhancement in the second network.
- Our SR feature enhancement is achieved with a residual between the input and estimated LR images in each iteration. Since the estimated LR image is affected not only by the reconstructed SR image but also by the estimated blur, this SR feature enhancement encourages the subsequent iterations to intensively learn erroneous features for both better SR and blur kernel estimation.
- In our proposed network, this residual learning is achieved in accordance with a back-projection manner. While the effectiveness of the back projection is demonstrated for non-blind SR with only the SR branch [5], our proposed network is designed to go along the back-projection manner for blind SR with the blur and SR branches. This back-projection through both the blur and SR branches improves the estimated blur kernel as well as the SR image.

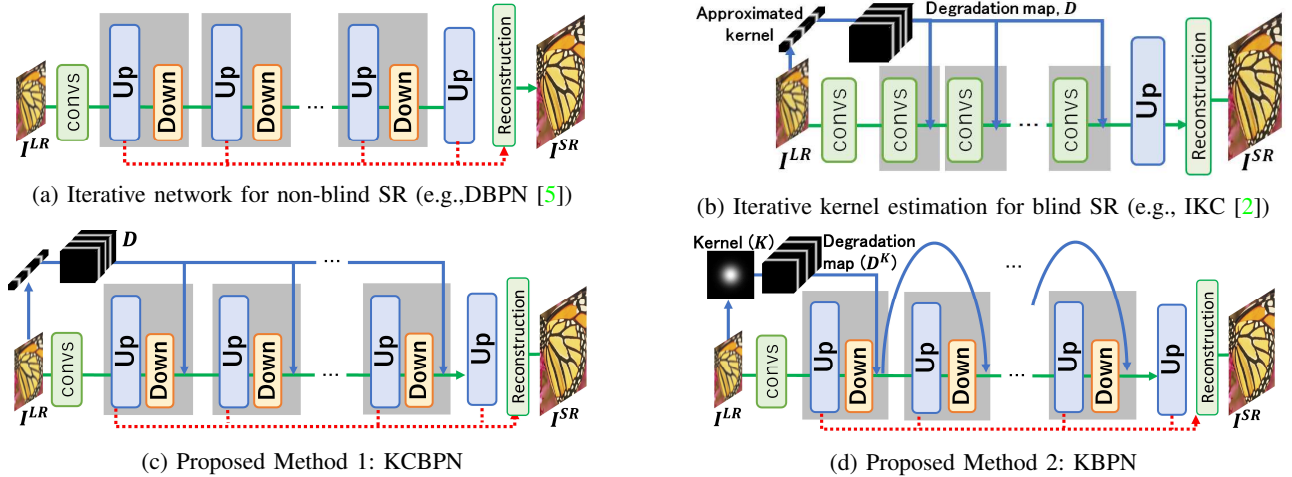


Fig. 2: Comparison of iterative SR networks. Iterative stages are enclosed by gray rectangles. (a) Non-blind SR with iterative up- and down-projections [5]. (b) Blind SR with kernel estimation [2]. (c) Our method 1 (KCBPN): Iterative up- and down-projections are integrated with kernel conditioning. (d) Our method 2 (KBPN): The image degradation process in Eq. (1) is explicitly modeled and employed for loss functions and SR feature enhancement. For highlighting the differences among (a), (b), and (c, d), several important details are omitted in this figure; see Fig. 4, for the detail of KBPN.

II. RELATED WORK

A. Non-kernel SR for a Predefined Degradation

In non-kernel SR, no blur-kernel representation is modeled. Many non-kernel SR methods are proposed with deep networks; e.g., light-weight networks [16]–[20], SR with reference images [21]–[23], edge preservation [24], [25], diverse image reconstruction [26]–[28], data augmentation for SR [29], attention mechanisms [30]–[34], similarity in feature maps [35], SR using adversarial training [36]–[38], iterative/recurrent mechanisms [5], [38]–[40], and implicit image functions [41]. Non-kernel SR differs from non-blind SR, where the degradation process is known in inference. All non-kernel SR methods are non-blind SR because they assume that only a single degradation process (e.g., bicubic downsampling with no blur in Eq. (1)) is used both in training and inference. This assumption inevitably hinders non-kernel SR from getting the best performance for arbitrarily-blurred images.

B. Kernel SR applicable to Any Degradations

For enabling a single SR model to be applicable to arbitrarily-degraded images, non-blind SR methods that accept a known blur kernel in inference are developed [6], [7], [42]–[44]. While they are beneficial as basic techniques and for several applications, this paper focuses on blind kernel SR.

We categorize blind SR methods using blur kernels as follows: (1) no kernel in networks, (2) kernel conditioning, and (3) direct image degradation.

1) *No kernel in networks*: While SR networks in this category have no blur kernel, training or input images are blurred or deblurred by a kernel. For example, training images degraded by various blurs are used for meta-transfer learning for efficient image-specific SR [11], [45]. A more variety of blurs (e.g., compression and sensor noise as well as the general Gaussian noise) improve the SR performance [46].

In SR extended by [47], training images degraded by various kernels are stochastically masked by different frequency bands for avoiding overfitting to any specific blur kernels. Various kernels estimated from real images are used for training in [48]. A SR network trained with this image set is expected to work well for real images.

Since these methods [11], [45], [47], [48] augment training images for robustness to blurs, this paper focuses more on SR networks with the kernel. While these methods [11], [45], [47], [48] use the kernel to downscale HR training images, correction filter [10] modifies an input LR image. The LR image is modified by the kernel estimated from it so that the modified LR image can be super-resolved well by non-kernel SR. While correction filter works for unknown kernels, it also has no kernel representation in the SR network.

2) *Kernel conditioning*: For SR robust to various blurs, an SR network is conditioned by a kernel in SRMD [7]. While SRMD is non-blind SR, this kernel conditioning is also useful for blind SR [2], [8]. Unlike non-blind SR in which the kernel is given, blind SR must estimate the kernel representation from the LR image. In [8], the LR image conditioned by the approximated kernel is fed into a network for predicting pixelwise differences between HR and SR images in training. In inference, the sum of the differences is minimized to determine the best SR image by optimizing the kernel. IKC [2] directly estimates the approximated kernel from the LR image. The estimated kernel conditions SR features with SFT [49] for feature improvement. In [13], a low-dimensional kernel estimator with reinforcement learning is proposed. The estimated low-dimensional kernel is employed by AdaIN [50] for controlling the SR process. DAN [15] integrates the networks of kernel representation estimation and SR for end-to-end training. DASR-Wang [4] improves a degradation kernel representation by contrastive learning [51]–[53].

TABLE I: Performance gains of non-kernel SR (DBPN [38]) by being trained with images degraded by various blur kernels. This method is suffixed by “-BI” (i.e., DBPN-BI), while DBPN is trained by only images with no blur (i.e., $\sigma \neq 0$). For comparison, blind kernel SR (IKC [2]) and its non-blind kernel version (SFTMD [2]) are shown. The performance is measured by PSNR. Red and blue scores indicate the best and the second-best, in each column, respectively.

Method	Set5	Set14	BSD100
DBPN	28.82	25.80	26.05
DBPN-BI	29.39	26.50	26.29
IKC	30.92	27.14	27.06

3) *Direct image degradation*: The above SR networks conditioned by the approximated kernel have two disadvantages: (i) the limited accuracy of the approximated kernel and (ii) the indirect degradation process with conditioning. Rather than unclear conditioning, the model-based representation with Eq. (1) may improve the representation ability.

In KernelGAN [9], the direct degradation expressed by Eq. (1) is estimated from the LR image based on feature similarity across different scales of the same images. FKP [12] stabilizes the kernel estimation process in the latent space. MANet [14] improves spatially-variant kernel estimation without increasing receptive fields. However, these methods [9], [12], [14] require an additional SR network using the estimated blur kernel. These kernel estimation and SR networks are not trained in an end-to-end manner.

Such end-to-end training is done in [3], [54]. In DRN [54], an SR image is downsampled to its LR image by the estimated degradation. In KOALANet [3], the raw kernel is estimated by the kernel estimator integrated with the SR network.

However, the aforementioned methods [3], [9], [12], [14], [54] employ the estimated degradation just for back-propagation (e.g., with MSE between the input and reconstructed LR images). In our proposed method, on the other hand, the image degradation is used for iteratively enhancing features for better SR reconstruction using iterative stages.

III. PRELIMINARY EXPERIMENTS: NON-BLIND SR IS IMPROVED BY VARIOUS KERNELS.

We conducted experiments using non-kernel SR with images degraded by various blur kernels. The aim is to explore how non-kernel SR is improved simply by being trained with these blurred images, as done in blind SR such as [2], [8]. While the similar experiments are done in [55], non-kernel SR and blind SR using kernel are compared with different conditions in [55]. That is, in [55], non-kernel SR is trained with several perceptual losses [56] as well as with a reconstruction MSE loss, but blind SR using kernel is trained with only a reconstruction loss. Such mixed conditions make it difficult to compare these non-kernel and kernelized methods fairly. In our experiments, on the other hand, both non-kernel and kernelized methods are trained with only a reconstruction MSE loss for fair comparison. In addition, we also compare non-kernel SR trained with variously-blurred images with its

original one trained only by bicubic downsampling with no blur. This comparison reveals the effect of the SR training with the variously-blurred images.

Training images are isotropically blurred by Gaussian kernels, each of whose variance is randomly selected from $[0.2, 4.0]$. Each test image is also isotropically blurred by the Gaussian kernel $\sigma \in \{1.3, 2.6\}$. The results are shown in Table I. We can see that DBPN-BI (trained by various blur kernels) is much better than the original DBPN trained only by bicubic downsampling with no blur. DBPN-BI is superior or comparable to IKC [2], which is one of the blind SR methods.

These results prod us into (i) revisiting a high-performance non-blind SR method (e.g., DBPN) and (ii) extending it to blind SR with blur kernels.

IV. PROPOSED METHODS

For organically integrating blind kernel estimation into any high-performance non-blind SR method, these blind and non-blind SR networks should have similar structures. Among potential combinations, we pay attention to iterative networks because of their abilities for augmenting and gradually revising features [2], [5], [38], [54]. Based on this motivation, this paper proposes the following two methods.

In the first method, kernel conditioning is integrated with an iterative end-to-end SR network, consisting of up- and down-projection modules [5], as shown in Fig. 2 c. For stabilizing both kernel estimation and conditioning, low-dimensional approximated kernels are employed, as proposed in [2], [8]. Different from IKC [2] (Fig. 2 b) where the iterative network is also used, the SR branch in our proposed network is based on iterative up-and-down samplings for SR feature enhancement with back projections [5], [38]. Furthermore, IKC consists of three separate networks, which are not trained in an end-to-end manner. We call this network the *Kernel-Conditioned Back-Projection Network* (KCBPN).

Since KCBPN is a simple integration of IKC and DBPN, KCBPN lacks several important components of kernelized SR introduced in Sec. II. First, its kernel representation is an approximated low-dimensional vector that may result in limited SR accuracy. Second, the approximated kernel makes it impossible to directly employ the image degradation expressed by Eq. (1). These problems are resolved in our second method (Fig. 2 d), which is called the *Kernelized Back-Projection Network* (KBPN). Unlike previous blind SR networks with the image degradation in which blurring and downsampling are integrated into one process [3], [9], [12], [14], [54], KBPN models Eq. (1) by separating blurring and downsampling sub-processes. This separate modeling with the simpler sub-processes allows us to simplify blind SR learning. More importantly, we propose to employ a residual between the reconstructed LR and its input LR images. While this residual is used for only back-propagation in previous blind SR methods, our method propagates it forward for learning erroneous features in the residual through the iterative mechanism.

In both KCBPN and KBPN, each iterative stage consists of upsampling, downsampling, blur estimation, and image degradation processes. SR features extracted in all iterative

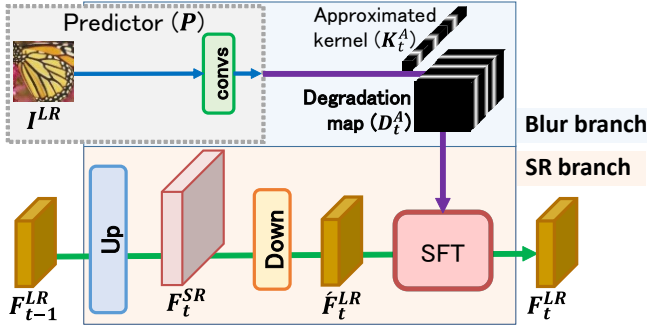


Fig. 3: t -th stage in KCBPN.

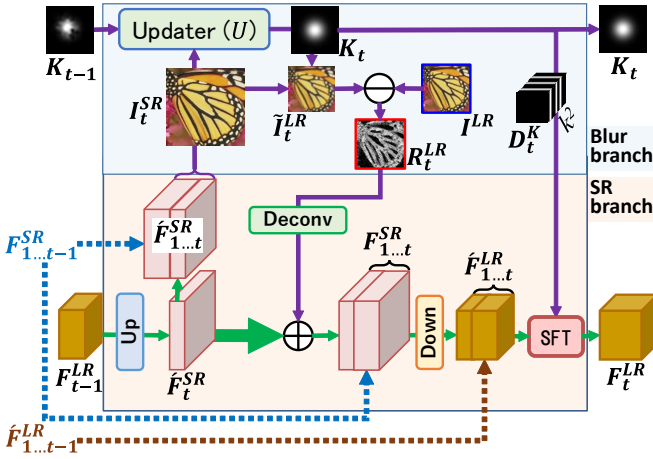


Fig. 4: t -th stage in KBPN.

stages (denoted by $F_{1,\dots,T}^{SR}$ where T denotes the number of stages) are finally concatenated channelwise and fed into the reconstruction layer with 3×3 convolution, as depicted by red dotted arrows in Fig. 2 c and d, for the final SR image (denoted by I^{SR}).

A. Kernel Conditioned Back-Projection Networks

The overall structure and each stage in KCBPN are illustrated in Figs. 2 c and 3, respectively. “LR features extracted in the $(t-1)$ -th stage (denoted by F_{t-1}^{LR})” and “the degradation map (denoted by D_t^A) extracted from an input LR image” are fed into the t -th stage. Its output is LR features (denoted by F_t^{LR}). D_t^A is the stretch of the low-dimensional vector of the kernel given by the kernel predictor, P .

In the SR branch, F_{t-1}^{LR} is up- and down-sampled for feature augmentation by extracting SR features, F_t^{SR} , and LR features, F_t^{LR} , as proposed in [5]. F_t^{LR} is conditioned with D_t^A by SFT [49] as follows:

$$\begin{aligned} \gamma &= S(\text{convs1}(\text{concat}(\hat{F}_t^{LR}, D_t^A))) \\ \beta &= \text{convs2}(\text{concat}(\hat{F}_t^{LR}, D_t^A)) \\ F_t^{LR} &= \hat{F}_t^{LR} \odot \gamma \oplus \beta, \end{aligned} \quad (2)$$

where convs1 and convs2 are two-layer CNNs. Their kernel size is 3×3 . Each conv layer is followed by LeakyReLU ($\alpha = 0.1$). $S(\cdot)$ denotes the sigmoid function.

B. Kernelized Back-Projection Networks

The overall structure and each stage of KBPN are shown in Fig. 2 d and Fig. 4, respectively. As with KCBPN, (i) the SR branch has up- and down-projection modules, and (ii) the kernel is fed into the SR branch from the blur branch. On the other hand, different from similar methods such as IKC and KCBPN, an SR image reconstructed in each stage is blurred by an estimated raw kernel K_t ($k \times k$ pixels) and downsampled by Eq. (1). KBPN consists of the following four steps.

In Step 1 of the t -th stage, the up-projection module extracts SR features from F_{t-1}^{LR} (i.e., LR features given by the $(t-1)$ -th stage). The upscaled features (denoted by \hat{F}_t^{SR}) are concatenated channelwise with $F_{1,\dots,t-1}^{SR}$ given by the previous stages. The concatenated features are denoted by $\hat{F}_{1,\dots,t}^{SR}$.

In Step 2, $\hat{F}_{1,\dots,t}^{SR}$ is used for reconstructing I_t^{SR} . As with the final reconstruction layer, this SR reconstruction is done by a 3×3 convolution layer. I_t^{SR} and K_{t-1} are fed into the blur updater, U , for updating K_{t-1} to K_t . I_t^{SR} is convolved by K_t for estimating \tilde{I}_t^{LR} .

Step 3 updates features by the residual between \tilde{I}_t^{LR} and the input LR image (I^{LR}). This residual, $R_t^{LR} = \tilde{I}_t^{LR} - I^{LR}$, represents how well I_t^{SR} and K_t are reconstructed. We propose to employ R_t^{LR} for enhancing SR features in the following iterations (i.e., F_τ^{SR} where $\tau = \{t+1, t+2, \dots, T\}$). For this **SR feature enhancement**, R_t^{LR} is provided from the blur branch to the SR branch so that \hat{F}_t^{SR} is enhanced. Let this enhanced SR feature be F_t^{SR} . We propose to design this SR feature enhancement as residual learning in which \hat{F}_t^{SR} is given through the identical mapping, indicated by the thick green arrow in Fig. 4. To this end, R_t^{LR} is upsampled by two conv layers and a deconv layer (indicated by “Deconv” in Fig. 4) for adding it to \hat{F}_t^{SR} elementwise. This residual feature feedback is done by elementwise-add in accordance with the original back-projection [57] and its network implementation [5], while they [5], [57] are designed with only the SR branch without the blur branch. For this elementwise-add operation, the channel size of R_t^{LR} is changed in this Deconv so that its channel size is equal to that of \hat{F}_t^{SR} . The kernel sizes of the first and second conv layers are 3×3 and 1×1 , respectively. The enhanced SR features (F_t^{SR}) is then concatenated channelwise with $F_{1,\dots,t-1}^{SR}$ given by the previous stages. This feature concatenation is inspired by dense connections in D-DBPN [5] to alleviate the vanishing gradient problem and encourage feature reuse. The elementwise-added features (denoted by $F_{1,\dots,t}^{SR}$) are fed into the down-projection module for getting the LR feature, $\hat{F}_{1,\dots,t}^{LR}$.

In Step 4, the updated kernel, K_t , is vectorized to a k^2 -dimensional vector and stretched to the degradation maps (denoted by D_t^K), as proposed in [7]. D_t^K is fed into SFT as the condition for updating $\hat{F}_{1,\dots,t}^{LR}$ to F_t^{LR} by Eq. (2). Finally, F_t^{LR} and K_t are provided to the $(t+1)$ -th stage.

The technical novelties in KBPN compared to the most related blind SR methods are summarized as follows:

- In SRMD [7], AMNet [13], DAN [15], DASR-Wang [4], and IKC [2], a low-dimensional kernel representation is used only for conditioning LR features, while KBPN also conditions the LR features by the estimated raw kernel.

- A raw kernel estimated in DRN [54] and KOALAnet [3] is used only for downscaling the reconstructed SR image. Then, a residual between the downscaled image and the input LR image is computed for back-propagation. In addition to this back-propagation, KBPN uses this residual (i.e., R_t^{LR}) also for enhancing SR features. Since pixels each of which has a higher value in R_t^{LR} can be regarded as erroneous pixels in \tilde{I}_t^{LR} , conditioning by R_t^{LR} encourages the next stage to explicitly learn features in order to focus on reconstructing these erroneous pixels. Integrating this feature enhancement with a back-projection manner [5], [57] between the blur and SR branches is our original scheme.
- Iterations in IKC [2] gradually get the kernel and SR image closer to their ground-truths. On the other hand, KBPN iterates the stages for feature enhancement (i.e., for producing different features) and utilizes the features extracted in all the stages for SR reconstruction. Furthermore, IKC is not trained in an end-to-end manner.

C. Loss Functions

In both KCBPN and KBPN, the following MSE loss is used for the SR image:

$$\mathcal{L}_{SR} = \frac{1}{CHW} \sum_c \sum_h \sum_w \left(I^{SR}(c, h, w) - I^{HR}(c, h, w) \right)^2, \quad (3)$$

where C , H , and W denote the channel size, height, and width of the HR and SR images, respectively.

The kernels estimated in the last T -th stage are considered to be the final estimations so that $K^A = K_T^A$ and $K = K_T$. These kernels are used for the kernel loss, denoted by \mathcal{L}_{KC} and \mathcal{L}_K in KCBPN and KBPN, respectively:

$$\mathcal{L}_{KC} = \frac{1}{a} \sum_i^a |K^A(i) - \bar{K}^A(i)|, \quad (4)$$

$$\mathcal{L}_K = \frac{1}{k^2} \sum_j^k \sum_i^k |K(j, i) - \bar{K}(j, i)|, \quad (5)$$

where \bar{K}^A and \bar{K} denote the ground-truth of K^A in KCBPN and K in KBPN, respectively. The dimension of K^A is a .

In addition, we propose to evaluate the LR image degraded from the output SR image I^{SR} in KBPN. This LR image is $\tilde{I}_T^{LR} = (I^{SR} * K) \downarrow_s$. The loss defined by the MSE between \tilde{I}_T^{LR} and I^{LR} is called the **LR loss**:

$$\mathcal{L}_{LR} = \frac{s^2}{CHW} \sum_c \sum_h \sum_w \left(\tilde{I}_T^{LR}(c, h, w) - I^{LR}(c, h, w) \right)^2 \quad (6)$$

While the LR loss is used also in [54], [58], these methods reconstruct the LR image from the SR image by non-linear downsampling neglecting the image degradation equation 1. In our method, on the other hand, the LR image is reconstructed by 1, which allows us to separate the whole degradation to the blurring and downsampling sub-processes for easier optimizations of these sub-processes.

In both KCBPN and KBPN, the weights of the SR loss (\mathcal{L}_{SR}) and the kernel loss (\mathcal{L}_{KC} in KCBPN and \mathcal{L}_K in KBPN) are 1 and 5, respectively. In KBPN, the weight of the LR loss, \mathcal{L}_{LR} , is 0.1.

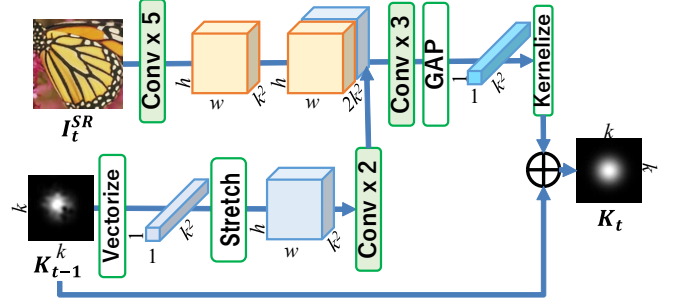


Fig. 5: Blur updater in KBPN.

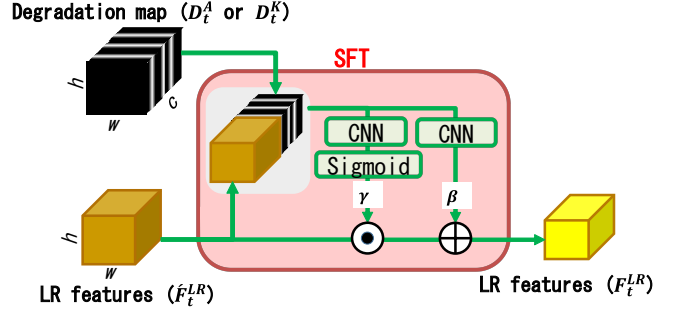


Fig. 6: Detail of SFT used in KCBPN and KBPN.

V. EXPERIMENTAL RESULTS

A. Detailed Implementation and Datasets

As with [21], in both KCBPN and KBPN, VGG-16 [62] is employed for feature extraction from an input LR image. More specifically, the first four convolution layers of VGG-16 without the pooling layers extract initial LR features, F_0^{LR} , from I^{LR} . The kernel sizes of the first and second conv layers are 3×3 and 1×1 , respectively. Up- and down-projection modules are designed in the same way as DBPN [5]. The reconstruction layer is a 3×3 conv layer with no activation. The sizes of initial LR and SR features (i.e., F_1^{LR} and F_1^{SR}) are $(c, w, h) = (64, \frac{W}{s}, \frac{H}{s})$ and $(c, w, h) = (64, W, H)$, respectively. The blur-kernel size k is 21. The kernel predictor P consisting of four convolutional layers and the last global average pooling layer in KCBPN and KBPN is identical to the one used in IKC [2]. Given the blur kernel with $k \times k$ pixels, the channel size of the output vector (denoted by c) is $c = 9$ and $c = k^2 = 441$ in KCBPN and KBPN, respectively. In KBPN, a k^2 -dimensional vector estimated by this blur predictor is reshaped to a $k \times k$ matrix. The architecture of the blur updater U in KBPN is shown in Fig. 5.

The detailed architectures of SFT [49] is illustrated in Fig. 6. For SFT, the degradation map (i.e., D_t^A in KCBPN and D_t^K in KBPN) and the LR feature (i.e., F_t^{LR}) are concatenated channelwise. This concatenated feature is fed into two convolution layers to get γ and β in parallel. The kernel size of each convolution layer is 3×3 . Each convolution layer is followed by LeakyReLU ($\alpha = 0.1$). With γ and β , the LR feature is updated to F_t^{LR} using Eq. (2).

We trained and evaluated two types of SR models inde-

TABLE II: Comparison with blind SR methods. Both training and test images are blurred by isotropic blur kernels. In each column, **red**, **blue**, and **green** denote the best, second-best, and third-best scores, respectively.

Method	σ	Set5		Set14		BSD100		σ	Set5		Set14		BSD100	
		PSNR	SSIM	PSNR	SSIM	PSNR	SSIM		PSNR	SSIM	PSNR	SSIM	PSNR	SSIM
DBPN [38]	0.2	23.44	0.714	19.91	0.584	20.52	0.570	2.6	26.80	0.772	24.90	0.660	25.17	0.630
DBPN-BI		26.45	0.809	22.15	0.669	23.02	0.655		28.05	0.804	25.87	0.698	25.60	0.648
IKC [2]		24.33	0.757	19.78	0.600	20.66	0.595		30.93	0.870	27.35	0.742	27.19	0.715
DAN [15]		25.44	0.777	20.92	0.589	21.76	0.609		29.56	0.848	26.31	0.726	26.73	0.701
KCBPN (stg7)		30.18	0.873	27.43	0.768	26.84	0.723		28.27	0.803	26.03	0.698	25.69	0.644
KBPN (stg7)		31.83	0.890	28.21	0.777	27.29	0.728		31.21	0.871	28.07	0.756	27.14	0.705
DBPN [38]	1.3	30.83	0.879	26.70	0.752	26.93	0.729	4.0	24.23	0.671	23.05	0.576	23.67	0.555
DBPN-BI		30.72	0.875	27.13	0.751	26.98	0.725		24.53	0.678	23.33	0.585	23.82	0.559
IKC [2]		30.90	0.878	26.92	0.751	26.92	0.726		25.75	0.740	24.23	0.622	24.54	0.601
DAN [15]		30.90	0.879	26.91	0.751	26.96	0.727		25.13	0.705	23.83	0.609	24.36	0.585
KCBPN (stg7)		30.78	0.876	27.80	0.767	27.15	0.720		25.11	0.696	23.61	0.593	24.06	0.565
KBPN (stg7)		32.33	0.895	28.60	0.783	27.61	0.733		26.15	0.736	24.67	0.635	24.76	0.594

TABLE III: Comparison with blind image-specific SR methods.

Method	σ	Set14 [59]		BSD100 [60]		σ	Set14 [59]		BSD100 [60]	
		PSNR	SSIM	PSNR	SSIM		PSNR	SSIM	PSNR	SSIM
(a) ZSSR [61] + KernelGAN [9] (Fully-blind)	$\frac{3.5}{\sqrt{2}}$	24.42	0.673	24.36	0.647	$\frac{4.5}{\sqrt{2}}$	25.17	0.669	25.24	0.652
(b) DBPN + Correction [10] (Fully-blind)		28.18	0.764	27.10	0.722		25.54	0.699	25.49	0.671
(c) KCBPN (stg7)		26.31	0.709	25.85	0.652		24.90	0.649	24.96	0.608
(d) KBPN (stg7)		28.26	0.764	27.29	0.713		26.76	0.710	26.23	0.660

pendently. The first and second models were trained with images blurred by isotropic and anisotropic Gaussian kernels, respectively. The numbers of the iterative stages are 7 and 4 for isotropic and anisotropic Gaussian blur kernels, respectively, in both KCBPN and KBPN. In addition, KBPN is evaluated also with 3 and 7 stages for anisotropic Gaussian blur kernels. All experiments were conducted with a scale factor of 4.

Training: 3,450 images in DIV2K [63] and Flickr2K [64] were used. All images were horizontally and vertically flipped for augmentation. The variance of the Gaussian blur kernel is randomly selected from $[0.2, 4.0]$. Adam [65] was used as an optimizer. The learning rate was initially 10^{-4} and reduced to 10^{-5} . The batch size was 8.

Evaluation: Set5 [66], Set14 [59], and BSD100 [60] are used for evaluation. For experiments shown in Tables II, III, and IV and Fig. 8, the test images are blurred by the isotropic Gaussian kernels with $\sigma \in \{0.2, 1.3, \frac{3.5}{\sqrt{2}}, 2.6, \frac{3.5}{\sqrt{2}}, 4.0\}$. The test images used in Table V and Fig. 9 are blurred by anisotropic Gaussians. The quantitative evaluation code we used is available in [67].

Codes and trained weights: All SOTA methods (i.e., DAN [68], ZSSR [69], Correction Filter [70], KOALANet [71], DASR-Gu [72], DASR-Wang [73], and FAIG [55]) are evaluated with the authors' codes and weights, except that IKC is evaluated with a publicly-available code [74] because its official code is unavailable. Since the trained weights given by the authors are used for a fair comparison, comparative methods differ between the results with isotropic and anisotropic blurs shown in Table II and Table V, respectively, depending on which blur is trained for which method. The scores of (a) and (b) in Table III are provided in [10]. Since all of these methods including KCBPN and KBPN are designed with reconstruction losses with no perceptual losses, they can be fairly compared.

TABLE IV: Ablation studies on KBPN with 7 stages. Both training and test images are blurred by isotropic blur kernels.

Method	Set5	Set14	BSD100
KBPN w/o enhancement	29.72	26.79	26.37
KBPN w/o L_{LR}	30.20	27.17	26.54
KBPN w/o L_K	30.15	27.01	26.48
KBPN w/o deconvs	30.06	27.07	26.59
KBPN	30.38	27.39	26.70

B. Quantitative Evaluation

Isotropic blur kernels: Table II shows PSNR and SSIM of blind SR methods. As the baselines, a non-kernel SR method (DBPN [38]) and its extension trained with various blur images (i.e., DBPN-BI) are shown. Since KCBPN and KBPN outperform DBPN-BI, which has no kernel representation, in all of $\sigma = \{0.2, 1.3, 2.6, 4.0\}$, the effectiveness of the kernel representation is validated. DBPN-BI, KCBPN, and KBPN are superior to IKC and DAN in $\sigma = 0.2$. In larger blurs (i.e., $\sigma = \{2.6, 4.0\}$), IKC and DAN are better than DBPN-BI and KCBPN in most cases. However, KBPN is the best in all datasets, metrics, and blurs except that KBPN is the second best in four cases (i.e., PSNR and SSIM of BSD100 in $\sigma = 2.6$, SSIM of Set5 in $\sigma = 4.0$, and SSIM of BSD100 in $\sigma = 4.0$, while the gaps from the best ones are small in all of these four cases).

vs blind image-specific SR: Table III¹ shows a comparison with blind image-specific methods, each of which is self-supervised by a test image. Kernel GAN [9] and Correction filter [10] are blind SR that requires an extra SR network. As the extra SR networks, ZSSR [61] and DBPN [5] were used.

¹ $\sigma = \{\frac{3.5}{\sqrt{2}}, \frac{4.5}{\sqrt{2}}\}$ are selected in accordance with [10].

TABLE V: Comparison with blind SR methods. Both training and test images are blurred by anisotropic blur kernels. In addition to PSNR and SSIM, NIQE and NRQM are also evaluated as perceptual quality metrics.

Method	σ_x/σ_y	Set5				Set14				BSD100			
		PSNR	SSIM	NIQE↓	NRQM	PSNR	SSIM	NIQE↓	NRQM	PSNR	SSIM	NIQE↓	NRQM
DBPN [38]	1.3/2.6	29.02	0.834	10.932	3.963	26.36	0.721	7.283	4.232	26.34	0.686	7.466	4.032
DBPN-B1		29.83	0.848	7.249	4.637	26.45	0.725	6.070	4.397	26.57	0.696	6.298	4.560
IKC [2]		30.14	0.861	8.227	4.932	27.08	0.742	6.752	4.761	26.93	0.713	7.161	5.067
KOALAnet [3]		30.49	0.866	9.227	4.387	26.98	0.735	7.209	4.216	26.80	0.702	7.357	4.188
DASR-Gu [75]		22.90	0.729	6.323	6.923	22.85	0.632	4.402	7.137	25.23	0.620	4.565	7.456
DASR-Wang [4]		30.66	0.869	8.406	4.831	27.00	0.737	7.035	4.491	26.90	0.707	7.221	4.607
FAIG [55]		30.02	0.866	10.263	5.227	27.11	0.744	7.071	4.641	26.81	0.717	7.199	5.033
KCBPN (stg4)		30.02	0.854	8.481	4.340	27.35	0.747	7.223	4.385	26.48	0.689	7.563	4.039
KBPN (stg3)		31.55	0.882	8.712	4.949	28.26	0.771	6.786	4.756	27.32	0.726	7.209	4.961
KBPN (stg4)		31.99	0.888	8.265	4.983	28.55	0.780	6.344	5.209	27.47	0.731	6.971	5.203
KBPN (stg7)	31.58	0.884	8.086	5.004	28.25	0.773	6.657	4.856	27.35	0.728	7.176	4.995	
DBPN [38]	2.6/4.0	25.40	0.721	11.192	2.499	23.79	0.607	10.036	2.346	24.29	0.587	9.922	2.397
DBPN-B1		27.11	0.772	8.376	3.443	24.93	0.650	7.384	3.502	25.08	0.619	7.567	3.340
IKC [2]		27.95	0.809	8.361	4.415	25.54	0.676	7.511	3.740	25.79	0.659	7.865	3.810
KOALAnet [3]		27.40	0.790	10.384	3.374	25.09	0.658	8.347	3.301	25.27	0.630	8.533	3.150
DASR-Gu [75]		21.91	0.682	6.883	3.688	21.96	0.583	5.916	3.397	24.37	0.578	5.950	3.601
DASR-Wang [4]		28.93	0.827	8.342	3.911	25.96	0.688	7.512	3.659	26.16	0.668	7.645	3.744
FAIG [55]		26.57	0.761	11.444	2.945	24.54	0.635	9.213	2.763	24.88	0.615	9.256	2.821
KCBPN (stg4)		25.85	0.732	10.174	2.768	24.48	0.636	8.853	2.849	24.58	0.598	9.171	2.620
KBPN (stg3)		29.20	0.825	10.425	4.172	26.54	0.704	7.563	3.971	26.09	0.662	7.636	3.950
KBPN (stg4)		28.30	0.809	13.869	3.820	26.44	0.703	7.783	3.831	25.87	0.653	7.851	3.700
KBPN (stg7)	28.82	0.815	10.103	4.076	26.58	0.704	7.526	4.031	26.07	0.662	7.592	4.024	

It can be seen that KBPN outperforms the image-specific blind SR methods in all datasets, metrics, and blurs, except that KBPN is the second best in two cases (i.e., SSIM of BSD100 in $\sigma = \frac{3.5}{\sqrt{2}}$ and $\sigma = \frac{4.5}{\sqrt{2}}$) in Table III. Furthermore, larger PSNR gains from the other methods are observed with a larger σ in Table III as well as in Table II.

Ablation study in KBPN: As demonstrated in Tables II and III, our main contributions exist in KBPN. In KBPN, our proposed SR feature enhancement and LR loss, \mathcal{L}_{LR} , are distinct components compared with other SR methods. In addition, we also evaluate the effect of the kernel loss, \mathcal{L}_K . Furthermore, the deconv layers in the connection from the blur branch to the SR branch are ablated. This ablation is done by bringing the destination of this connection to the path between $\hat{F}_{1,\dots,t}^{LR}$ and SFT (see Fig. 2d). The effects of these three components are verified in the ablation study.

The effects of these four components are shown in Table IV. The PSNR scores are the mean values of $\sigma = \{0.2, 1.3, 2.6, 4.0\}$ of all the datasets. We can see that all of the SR feature enhancement, L_{LR} , L_K , and the deconv layers can improve the SR performance in all cases in Table IV.

Anisotropic blur kernels: Blind SR methods trained by anisotropically-blurred images are shown in Table V. In addition to PSNR and SSIM, two perceptual scores (i.e., NIQE [76] and NRQM [77]) are assessed. Unlike other metrics, a lower value is better in NIQE. Different from the results of isotropically-blurred images, it is difficult to choose a method that outperforms all others in all metrics. We can see the following observations:

- In the distortion scores (i.e., PSNR and SSIM), either of KBPNs with the different numbers of stages is the best in most cases; only in PSNR and SSIM of BSD100 in $\sigma_x/\sigma_y = 2.6/4.0$, DASR-Wang is the best. The second and third bests are also observed in KBPN.

TABLE VI: Computational cost: the number of parameters (Mega)

	KCBPN (stg4)	KBPN (stg4)	IKC	KOALAnet
Params	8.0	61.2	9.1	6.5
	AMNet	DAN	DASR-Gu	DASR-Wang
Params	22.0	4.3	16.7	6.0

- In the perceptual scores, DASR-Gu [75] is the best in a smaller blur (i.e., $\sigma_x/\sigma_y = 1.3/2.6$), while KBPN follows DASR-Gu so that KBPN with four stages gets two second-best scores and two third-best scores. In a larger blur, KBPN with seven stages gets two best scores and two third-best scores, while DASR-Gu is the best in three cases. While the perceptual scores of DASR-Gu are better in many cases, its distortion scores (PSNR and SSIM) are much worse than KBPN; for example, the PSNR scores of DASR-Gu and KBPN with four stages are 23.20 and 28.10, respectively, on average over all cases shown in Table V.

Based on the above observations, we can conclude that KBPN is the best in terms of the trade-off between the distortion and perceptual scores, especially in a larger blur, as with in Table II.

Computational Cost: While iterative stages in KBPN overall improve the SR quality, their computational cost is . For verifying this limitation compared with other blind SR methods, Table VI shows the number of parameters large².

²While the iterative process in IKC and DAN is achieved by recurrently employing a single module, KBPN consists of multiple sequentially-connected modules so that the number of the iterations is equal to the one of the modules. Since the single module is shared among all the iteration processes in IKC and DAN, the module size can be reduced compared with the computational cost. KBPN, on the other hand, consists of multiple sequentially-connected modules for improving the performance with the large network capacity.

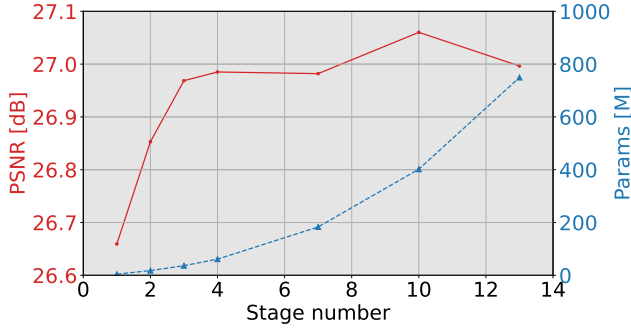


Fig. 7: Relationship between PSNR and the number of parameters changed according to the number of stages in KBPN. The horizontal axis indicates the number of stages. The left and right vertical axes (which correspond to red and blue line graphs, respectively) indicate PSNR and the number of parameters, respectively. These PSNR scores are the mean scores with anisotropic blurs of $\sigma_x \in \{0.2, 1.3, 2.6, 4.0\}$ and $\sigma_y \in \{0.2, 1.3, 2.6, 4.0\}$ on the BSD100 dataset.

The relationship between the SR performance and the number of stages (denoted by N_s) in KBPN is shown in Fig. 7. While the number of parameters becomes bigger as N_s increases, the SR performance (i.e., PSNR) is almost saturated at $N_s = 3$. In particular, the PSNR score decreases after the score is the largest at $N_s = 10$ probably due to overfitting.

C. Visual Results with Images Blurred by Isotropic Blurs

Figure 8 shows the SR results of KCBPN and KBPN in which both training and test images are isotropically blurred. All images in Fig. 8 are cropped from their original SR images for detailed observations. For comparison, the results of DBPN [5] as non-blind SR, its extension trained by various blur kernels (DBPN-BI) as non-kernel SR, IKC [2], and DAN [15] are shown. The PSNR score of each SR image is also shown in this figure. In most examples, KCBPN and KBPN can reconstruct better images as validated qualitatively and quantitatively. While other SOTA methods (IKC and DAN) reconstruct sharper boundaries, their PSNR scores are much worse than KCBPN and KBPN because the boundaries reconstructed by IKC and DAN are unrealistically jagged.

D. Visual Results with Images Blurred by Anisotropic Blurs

Figure 9 shows the SR images of KCBPN and KBPN reconstructed from LR images degraded by anisotropic Gaussian kernels. The PSNR and NIQE scores are shown with each SR result. For comparison, DBPN-BI, IKC [2], DASR–Gu [75], and DASR–Wang [4] are also shown. It can be seen that KBPN is superior to the other methods in terms of the trade-off between PSNR (i.e., image distortion) and NIQE (i.e., perceptual quality), and KBPN tended to emphasize scene edges more clearly, which is an important property in terms of actual perceptual quality.

E. Visualization of Estimated Kernels

Figure 10 shows examples of blur kernels estimated in test images blurred by isotropic Gaussian kernels ($\sigma = 1.3, 2.6$)

and anisotropic Gaussian kernels ($\sigma_x/\sigma_y = 1.3/2.6, 1.3/4.0$). These sample test images contain both complex and less textured images. Since such complex and less textures make kernel estimation less and more difficult, respectively, these images are appropriate for understanding the pros and cons of our proposed method. The kernels estimated with more complex anisotropic Gaussian blurs ($\sigma_x/\sigma_y = 1.3/4.0$) are directionally correct, but the estimated variance is not accurate. More improvement of this kernel estimation is important for future work. By enhancing the kernel estimation more, it is expected that the quality of KBPN for the anisotropic Gaussian blurs shown in Table III can be improved more.

F. Feature Representation Analysis

In [38], feature maps extracted in different iterative stages are visualized for demonstrating that a variety of features can be extracted. Such feature maps are visualized also in our KBPN for verifying whether or not our iterative stages with the proposed SR feature enhancement can extract various features. SR feature maps $F_{1..t}^{SR}$ and LR residual maps R_t^{LR} in different stages are shown in Fig. 11. Each feature map is converted to a grayscale image for visualization.

We can see that KBPN extracts a variety of feature maps in $F_{1..t}^{SR}$. The first stage tends to represent low-frequency features, while the last stage represents high-frequency features.

In $R_t^{LR} = \tilde{I}_t^{LR} - I^{LR}$ where $\tilde{I}_t^{LR} = (I_t^{SR} * K_t) \downarrow_s$, pixelwise values decrease in the later stages. This is evidence that features extracted in the later stages are better optimized for estimating I^{SR} and K . The decrease in value is noticeable in the edge lines of objects. This also suggests that high-frequency features are represented more in the later stages than in the earlier stages; since the high-frequency features allow us to reconstruct the edge lines sharper, the residuals in the edge lines become smaller.

Note that pixelwise values in $R_t^{LR} = \tilde{I}_t^{LR} - I^{LR}$ are larger in all the stages (i.e., $t \in \{1, 2, 3, 4\}$) because the LR loss is used only in the final output (i.e., $\tilde{I}^{LR} = (I^{SR} * K) \downarrow_s$) so that the final residual $R^{LR} = \tilde{I}^{LR} - I^{LR}$ is successfully reduced. In KBPN, the LR loss is not used in all the stages for learning a variety of features in these stages; if R_t^{LR} is converged to zero by the LR loss in each stage, \tilde{I}_t^{LR} in all stages become similar. Such uniform learning goals disturb all the stages to learn a variety of features.

VI. LIMITATION

We have confirmed that KBPN exhibits performance that surpasses the SOTA methods in blind SR. However, our approach has the following limitations:

The number of parameters is substantial compared to conventional methods. Nevertheless, considering the recent trends in the development of foundation models [78] and the advancements in computational resources, we believe that this is not a concern for offline applications. If our approach were to be introduced to edge devices, strategies such as pruning the dense connection, which can become a bottleneck in model size, are considered effective.

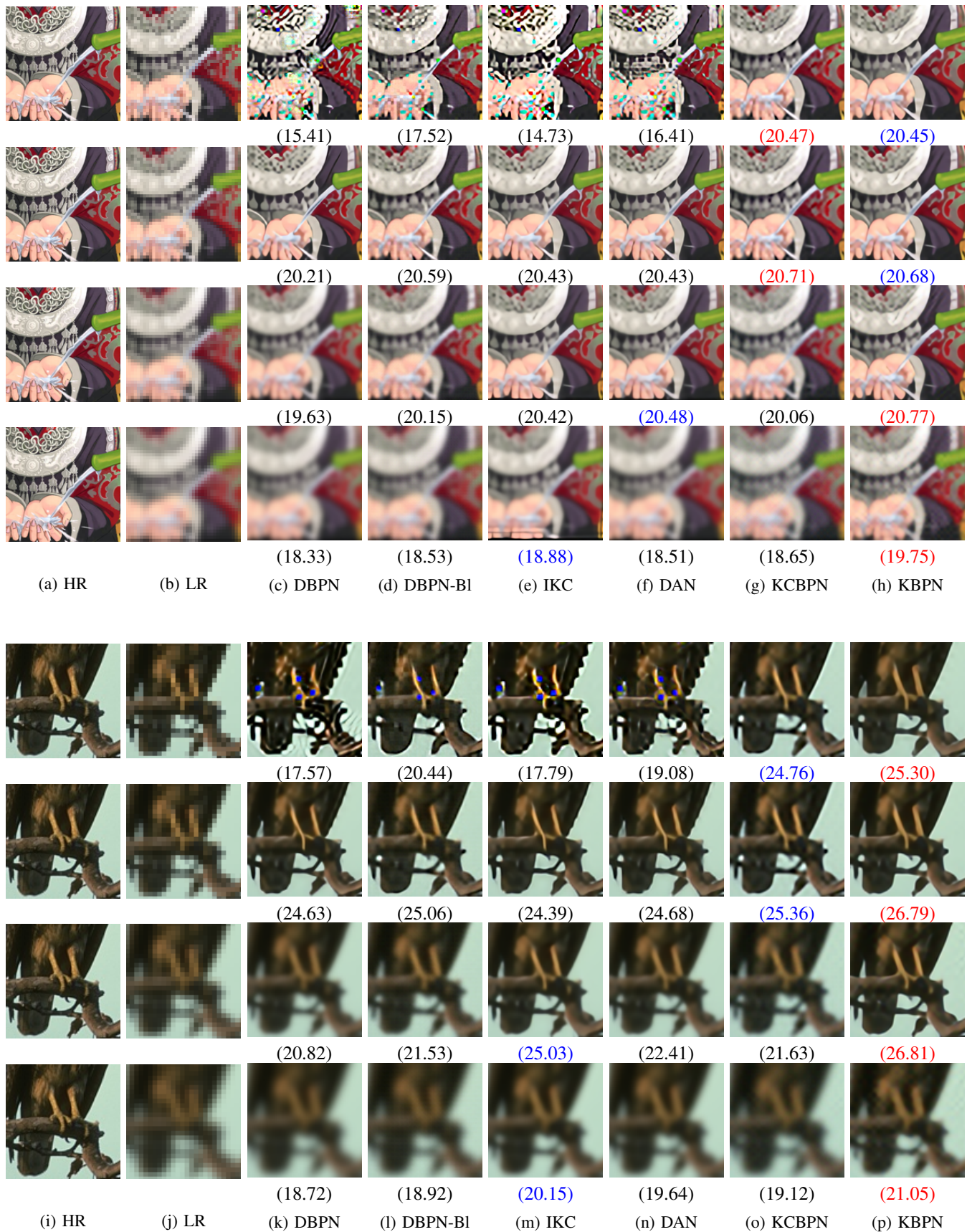


Fig. 8: Visual SR comparison. HR images are degraded with the isotropic Gaussian kernels ($\sigma \in \{0.2, 1.3, 2.6, 4.0\}$). The first, second, third and fourth rows show the results of $\sigma = 0.2, 1.3, 2.6, 4.0$, respectively. A value in each parenthesis is PSNR. The best and the second-best scores are colored by red and blue, respectively, in each row.

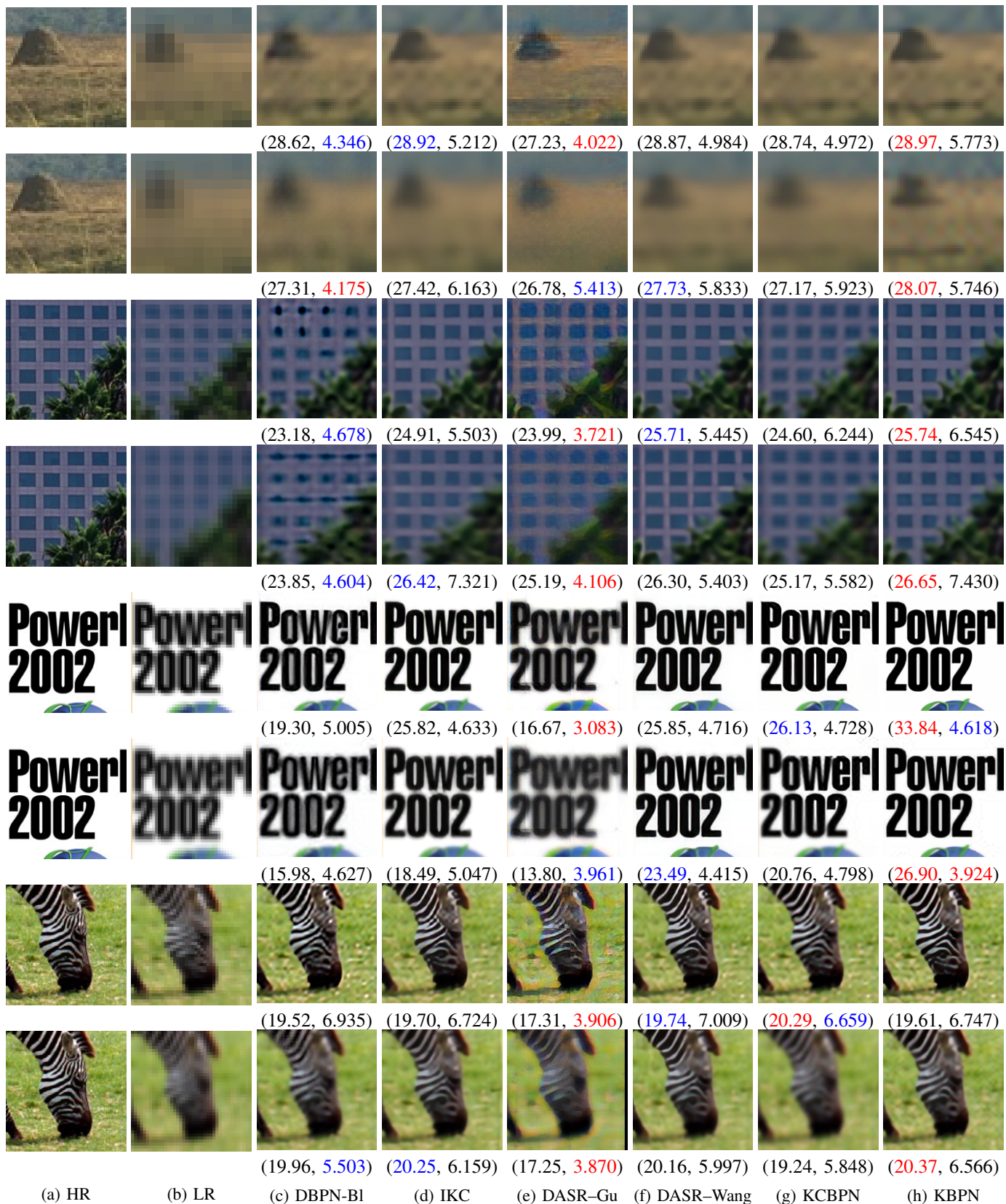


Fig. 9: Visual SR comparison. In each example, The first and second rows show the results of test images degraded with $\sigma_x/\sigma_y = 1.3/2.6$ and $2.6/4.0$, respectively. Values in each parenthesis are (PSNR, NIQE \downarrow). The best and the second-best scores are colored by red and blue, respectively, in each row.

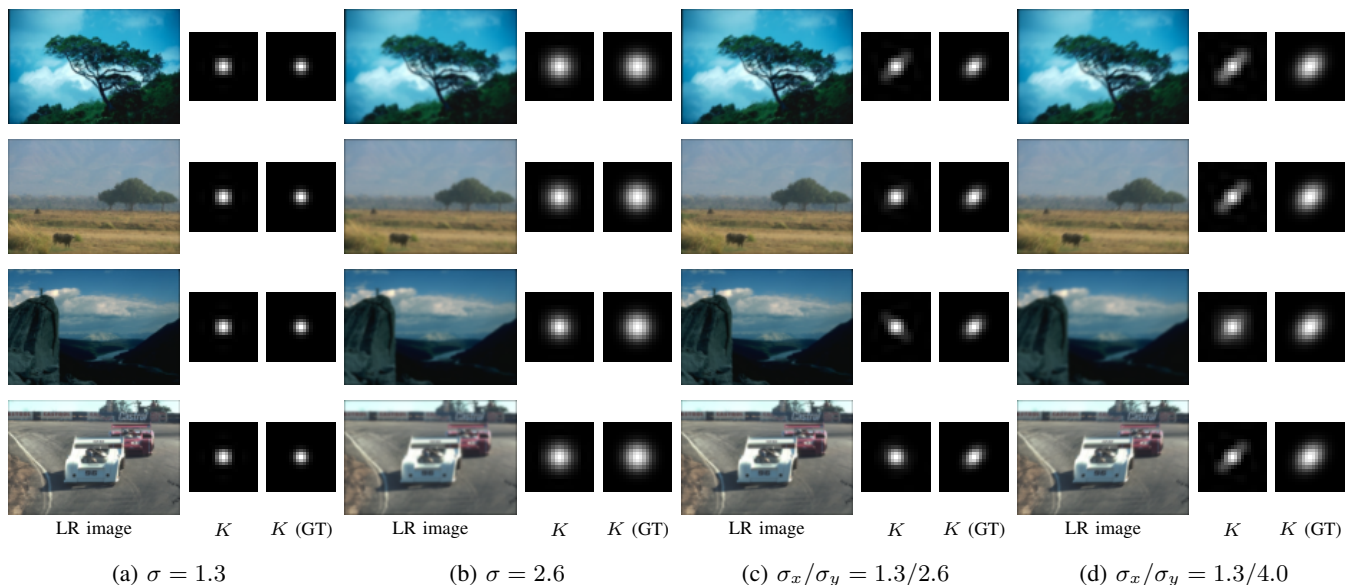


Fig. 10: Visualization of estimated kernels (K) in KBPN. The ground-truth kernels are shown in the rightmost column in each of (a), (b), (c), and (d). Note that these LR images are difficult examples for kernel estimation because less textures are captured so that textureless sky and ground are widely observed.

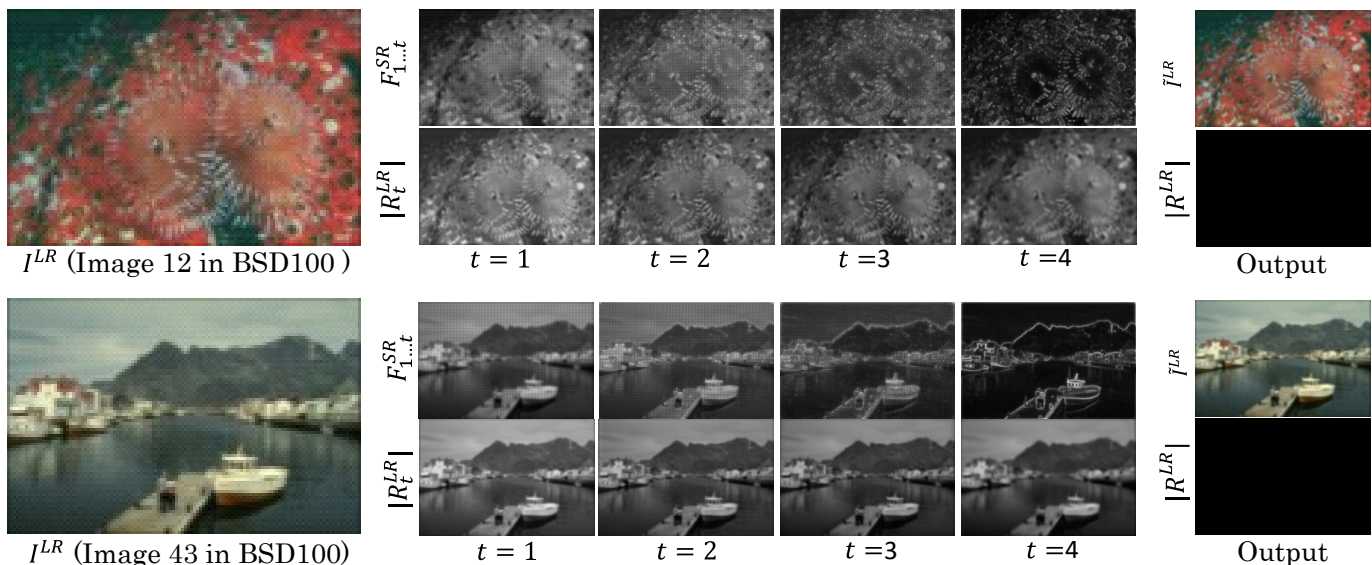


Fig. 11: Visualization results of the SR feature maps $F_{1,\dots,t}^{SR}$ and the LR image residuals $|R_t^{LR}|$ of in KBPN with 4 stages. For reference, the LR image residual computed with the output SR image I^{SR} (i.e., $|R^{LR}| = |\tilde{I}^{LR} - I^{LR}|$ where $\tilde{I}^{LR} = (I^{SR} * K) \downarrow_s$) is also shown in the lower row of the rightmost column. I^{LR} in this figure are generated with $\sigma_x/\sigma_y = 1.3/2.6$.

While KBPN demonstrates robustness against degradation caused by blur, it does not model degradation due to noise, thus not guaranteeing robustness in such scenarios. To address this issue, it is possible to train the model to handle various forms of degradation, such as the pure synthetic data generation technique [79] and the implicit degradation representation [80].

VII. CONCLUDING REMARKS

This paper proposed blind super-resolution methods, KCBPN and KBPN. They have blur and SR branches. Blur kernels estimated in the blur branch are employed not only for back-propagation using the kernel loss but also for SR feature

enhancement in the SR branch. In addition to the kernel loss, the LR loss is proposed to train KBPN with the estimated raw kernel. Furthermore, KBPN achieves further SR feature enhancement using a residual between the input LR image and the one reconstructed by Eq. (1).

Future work includes the improvement of the base SR and blur estimation networks. Since only artificial blurs are used for training KCBPN and KBPN as well as other blind SR methods, difficulty in real-image SR is a possible limitation. Further improvement may be achieved by integrating KCBPN and KBPN with a more variety of blurs [46].

This work is partly supported by JSPS KAKENHI Grant Numbers 19K12129 and 22H03618.

REFERENCES

- [1] R. Timofte *et al.*, “NTIRE 2018 challenge on single image super-resolution: Methods and results,” in *CVPR Workshops*, 2018. 1
- [2] J. Gu, H. Lu, W. Zuo, and C. Dong, “Blind super-resolution with iterative kernel correction,” in *CVPR*, 2019. 1, 2, 3, 4, 5, 6, 7, 8
- [3] S. Y. Kim, H. Sim, and M. Kim, “KoalaNet: Blind super-resolution using kernel-oriented adaptive local adjustment,” in *CVPR*, 2021. 1, 3, 5, 7
- [4] L. Wang, Y. Wang, X. Dong, Q. Xu, J. Yang, W. An, and Y. Guo, “Unsupervised degradation representation learning for blind super-resolution,” in *CVPR*, 2021. 1, 2, 4, 7, 8
- [5] M. Haris, G. Shakhnarovich, and N. Ukita, “Deep back-projection networks for super-resolution,” in *CVPR*, 2018. 1, 2, 3, 4, 5, 6, 8
- [6] G. Riegler, S. Schuler, M. R  ther, and H. Bischof, “Conditioned regression models for non-blind single image super-resolution,” in *ICCV*, 2015. 1, 2
- [7] K. Zhang, W. Zuo, and L. Zhang, “Learning a single convolutional super-resolution network for multiple degradations,” in *CVPR*, 2018. 1, 2, 4
- [8] V. Cornill  re, A. Djelouah, Y. Wang, O. Sorkine-Hornung, and C. Schroers, “Blind image super-resolution with spatially variant degradations,” *ACM Trans. Graph.*, vol. 38, no. 6, pp. 166:1–166:13, 2019. 1, 2, 3
- [9] S. Bell-Kligler, A. Shocher, and M. Irani, “Blind super-resolution kernel estimation using an internal-gan,” in *NuerIPS*, 2019. 1, 3, 6
- [10] S. A. Hussein, T. Tիրer, and R. Giryes, “Correction filter for single image super-resolution: Robustifying off-the-shelf deep super-resolvers,” in *CVPR*, 2020. 1, 2, 6
- [11] J. W. Soh, S. Cho, and N. I. Cho, “Meta-transfer learning for zero-shot super-resolution,” in *CVPR*, 2020. 1, 2
- [12] J. Liang, K. Zhang, S. Gu, L. V. Gool, and R. Timofte, “Flow-based kernel prior with application to blind super-resolution,” in *CVPR*, 2021. 1, 3
- [13] Z. Hui, J. Li, X. Wang, and X. Gao, “Learning the non-differentiable optimization for blind super-resolution,” in *CVPR*, 2021. 1, 2, 4
- [14] J. Liang, G. Sun, K. Zhang, L. V. Gool, and R. Timofte, “Mutual affine network for spatially variant kernel estimation in blind image super-resolution,” in *ICCV*, 2021. 1, 3
- [15] Z. Luo, Y. Huang, S. Li, L. Wang, and T. Tan, “Unfolding the alternating optimization for blind super resolution,” in *NeurIPS*, H. Larochelle, M. Ranzato, R. Hadsell, M. Balcan, and H. Lin, Eds., 2020. 1, 2, 4, 6, 8
- [16] W. Lee, J. Lee, D. Kim, and B. Ham, “Learning with privileged information for efficient image super-resolution,” in *ECCV*, 2020. 2
- [17] H. Li, C. Yan, S. Lin, X. Zheng, B. Zhang, F. Yang, and R. Ji, “PAMS: quantized super-resolution via parameterized max scale,” in *ECCV*, 2020. 2
- [18] X. Luo, Y. Xie, Y. Zhang, Y. Qu, C. Li, and Y. Fu, “Latticenet: Towards lightweight image super-resolution with lattice block,” in *ECCV*, 2020. 2
- [19] J. Xin, N. Wang, X. Jiang, J. Li, H. Huang, and X. Gao, “Binarized neural network for single image super resolution,” in *ECCV*, 2020. 2
- [20] R. Lee, L. Dudziak, M. S. Abdelfattah, S. I. Venieris, H. Kim, H. Wen, and N. D. Lane, “Journey towards tiny perceptual super-resolution,” in *ECCV*, 2020. 2
- [21] Z. Zhang, Z. Wang, Z. L. Lin, and H. Qi, “Image super-resolution by neural texture transfer,” in *CVPR*, 2019. 2, 5
- [22] Y. Zhang, Z. Zhang, S. DiVerdi, Z. Wang, J. Echevarria, and Y. Fu, “Texture hallucination for large-factor painting super-resolution,” in *ECCV*, 2020. 2
- [23] X. Yan, W. Zhao, K. Yuan, R. Zhang, Z. Li, and S. Cui, “Towards content-independent multi-reference super-resolution: Adaptive pattern matching and feature aggregation,” in *ECCV*, 2020. 2
- [24] W. Yang, J. Feng, J. Yang, F. Zhao, J. Liu, Z. Guo, and S. Yan, “Deep edge guided recurrent residual learning for image super-resolution,” *IEEE Trans. Image Process.*, vol. 26, no. 12, pp. 5895–5907, 2017. 2
- [25] C. Ma, Y. Rao, Y. Cheng, C. Chen, J. Lu, and J. Zhou, “Structure-preserving super resolution with gradient guidance,” in *CVPR*, 2020. 2
- [26] J. He, C. Dong, and Y. Qiao, “Modulating image restoration with continual levels via adaptive feature modification layers,” in *CVPR*, 2019. 2
- [27] Y. Bahat and T. Michaeli, “Explorable super resolution,” in *CVPR*, 2020. 2
- [28] A. Lugmayr, M. Danelljan, L. V. Gool, and R. Timofte, “SrfFlow: Learning the super-resolution space with normalizing flow,” in *ECCV*, 2020. 2
- [29] J. Yoo, N. Ahn, and K. Sohn, “Rethinking data augmentation for image super-resolution: A comprehensive analysis and a new strategy,” in *CVPR*, 2020. 2
- [30] Y. Zhang, K. Li, K. Li, L. Wang, B. Zhong, and Y. Fu, “Image super-resolution using very deep residual channel attention networks,” in *ECCV*, 2018. 2
- [31] Y. Zhang, K. Li, K. Li, B. Zhong, and Y. Fu, “Residual non-local attention networks for image restoration,” in *ICLR*, 2019. 2
- [32] M. Sukanuma, X. Liu, and T. Okatani, “Attention-based adaptive selection of operations for image restoration in the presence of unknown combined distortions,” in *CVPR*, 2019. 2
- [33] T. Dai, J. Cai, Y. Zhang, S. Xia, and L. Zhang, “Second-order attention network for single image super-resolution,” in *CVPR*, 2019. 2
- [34] B. Niu, W. Wen, W. Ren, X. Zhang, L. Yang, S. Wang, K. Zhang, X. Cao, and H. Shen, “Single image super-resolution via a holistic attention network,” in *ECCV*, 2020. 2
- [35] J. Johnson, A. Alahi, and L. Fei-Fei, “Perceptual losses for real-time style transfer and super-resolution,” in *ECCV*, 2016. 2
- [36] C. Ledig, L. Theis, F. Husz  r, J. Caballero, A. Cunningham, A. Acosta, A. Aitken, A. Tejani, J. Totz, Z. Wang *et al.*, “Photo-realistic single image super-resolution using a generative adversarial network,” in *CVPR*, 2017. 2
- [37] M. S. M. Sajjadi, B. Sch  lkopf, and M. Hirsch, “Enhancenet: Single image super-resolution through automated texture synthesis,” in *ICCV*, 2017. 2
- [38] M. Haris, G. Shakhnarovich, and N. Ukita, “Deep back-projection networks for single image super-resolution,” *IEEE Trans. Pattern Anal. Mach. Intell.*, vol. 43, no. 12, pp. 4323–4337, 2021. 2, 3, 6, 7, 8
- [39] X. Yang, H. Mei, J. Zhang, K. Xu, B. Yin, Q. Zhang, and X. Wei, “DRFN: deep recurrent fusion network for single-image super-resolution with large factors,” *IEEE Trans. Multimedia.*, vol. 21, no. 2, pp. 328–337, 2019. 2
- [40] Y. Zhang, P. Wang, F. Bao, X. Yao, C. Zhang, and H. Lin, “A single-image super-resolution method based on progressive-iterative approximation,” *IEEE Trans. Multimedia.*, vol. 22, no. 6, pp. 1407–1422, 2020. 2
- [41] H. Hu, Y. Chen, J. Xu, S. Borse, H. Cai, F. Porikli, and X. Wang, “Learning implicit feature alignment function for semantic segmentation,” in *CVPR*, 2022. 2
- [42] K. Zhang, W. Zuo, and L. Zhang, “Deep plug-and-play super-resolution for arbitrary blur kernels,” in *CVPR*, 2019. 2
- [43] Y. Xu, S. R. Tseng, Y. Tseng, H. Kuo, and Y. Tsai, “Unified dynamic convolutional network for super-resolution with variational degradations,” in *CVPR*, 2020. 2
- [44] K. Zhang, L. V. Gool, and R. Timofte, “Deep unfolding network for image super-resolution,” in *CVPR*, 2020. 2
- [45] S. Park, J. Yoo, D. Cho, J. Kim, and T. H. Kim, “Fast adaptation to super-resolution networks via meta-learning,” in *ECCV*, 2020. 2
- [46] K. Zhang, J. L. L. V. Gool, and R. Timofte, “Designing a practical degradation model for deep blind image super-resolution,” in *ICCV*, 2021. 2, 11
- [47] M. E. Helou, R. Zhou, and S. S  sstrunk, “Stochastic frequency masking to improve super-resolution and denoising networks,” in *ECCV*, 2020. 2
- [48] R. Zhou and S. S  sstrunk, “Kernel modeling super-resolution on real low-resolution images,” in *ICCV*, 2019. 2
- [49] X. Wang, K. Yu, C. Dong, and C. Change Loy, “Recovering realistic texture in image super-resolution by deep spatial feature transform,” in *CVPR*, 2018. 2, 4, 5
- [50] X. Huang and S. J. Belongie, “Arbitrary style transfer in real-time with adaptive instance normalization,” in *ICCV*, 2017. 2
- [51] T. Chen, S. Kornblith, M. Norouzi, and G. E. Hinton, “A simple framework for contrastive learning of visual representations,” in *ICML*, 2020. 2
- [52] A. Dosovitskiy, J. T. Springenberg, M. A. Riedmiller, and T. Brox, “Discriminative unsupervised feature learning with convolutional neural networks,” in *NIPS*, 2014. 2
- [53] K. He, H. Fan, Y. Wu, S. Xie, and R. B. Girshick, “Momentum contrast for unsupervised visual representation learning,” in *CVPR*, 2020. 2
- [54] Y. Guo, J. Chen, J. Wang, Q. Chen, J. Cao, Z. Deng, Y. Xu, and M. Tan, “Closed-loop matters: Dual regression networks for single image super-resolution,” in *CVPR*, 2020. 3, 5
- [55] L. Xie, X. Wang, C. Dong, Z. Qi, and Y. Shan, “Finding discriminative filters for specific degradations in blind super-resolution,” in *NeurIPS*, 2021. 3, 6, 7

- [56] Y. Blau *et al.*, “The 2018 PIRM challenge on perceptual image super-resolution,” in *ECCV Workshops*, L. Leal-Taixé and S. Roth, Eds., 2018. 3
- [57] M. Irani and S. Peleg, “Improving resolution by image registration,” *CVGIP*, vol. 53, no. 3, pp. 231–239, 1991. 4, 5
- [58] Y. Yuan, S. Liu, J. Zhang, Y. Zhang, C. Dong, and L. Lin, “Unsupervised image super-resolution using cycle-in-cycle generative adversarial networks,” in *CVPR Workshop*, 2018. 5
- [59] R. Zeyde, M. Elad, and M. Protter, “On single image scale-up using sparse-representations,” in *Curves and Surfaces*, 2010. 6
- [60] D. Martin, C. Fowlkes, D. Tal, and J. Malik, “A database of human segmented natural images and its application to evaluating segmentation algorithms and measuring ecological statistics,” in *ICCV*, 2001. 6
- [61] A. Shocher, N. Cohen, and M. Irani, ““zero-shot” super-resolution using deep internal learning,” in *CVPR*, 2018. 6
- [62] K. Simonyan and A. Zisserman, “Very deep convolutional networks for large-scale image recognition,” in *ICLR*, 2015. 5
- [63] E. Agustsson and R. Timofte, “Ntire 2017 challenge on single image super-resolution: Dataset and study,” in *NTIRE (CVPRW)*, 2017. 6
- [64] R. Timofte, E. Agustsson, L. Van Gool, M.-H. Yang, and L. Zhang, “Ntire 2017 challenge on single image super-resolution: Methods and results,” in *NTIRE (CVPRW)*, 2017. 6
- [65] D. P. Kingma and J. Ba, “Adam: A method for stochastic optimization,” in *ICLR*, 2015. 6
- [66] M. Bevilacqua, A. Roumy, C. Guillemot, and M. Alberi-Morel, “Low-complexity single-image super-resolution based on nonnegative neighbor embedding,” in *BMVC*, 2012. 6
- [67] Github, “The pirm challenge on perceptual super-resolution,” <https://github.com/roimehrez/PIRM2018>. 6
- [68] —, “Dan: Unfolding the alternating optimization for blind super resolution,” <https://github.com/greatlog/DAN>. 6
- [69] —, ““zero-shot” super-resolution using deep internal learning (zssr),” <https://github.com/assafshocher/ZSSR>. 6
- [70] —, “Correction filter for single image super-resolution: Robustifying off-the-shelf deep super-resolvers,” <https://github.com/shadyabh/Correction-Filter>. 6
- [71] —, “Koalanel: Blind super-resolution using kernel-oriented adaptive local adjustment,” <https://github.com/hjSim/KOALAnet>. 6
- [72] —, “Dasr: Unsupervised real-world image super resolution via domain-distance aware training,” <https://github.com/ShuhangGu/DASR>. 6
- [73] —, “Dasr: Unsupervised degradation representation learning for blind super-resolution,” <https://github.com/LongguangWang/DASR>. 6
- [74] —, “Ikc: Blind super-resolution with iterative kernel correction,” <https://github.com/yuanjunchai/IKC>. 6
- [75] Y. Wei, S. Gu, Y. Li, R. Timofte, L. Jin, and H. Song, “Unsupervised real-world image super resolution via domain-distance aware training,” in *CVPR*, 2021. 7, 8
- [76] A. Mittal, R. Soundararajan, and A. C. Bovik, “Making a “completely blind” image quality analyzer,” *IEEE Signal Process. Lett.*, vol. 20, no. 3, pp. 209–212, 2013. 7
- [77] C. Ma, C. Yang, X. Yang, and M. Yang, “Learning a no-reference quality metric for single-image super-resolution,” *Comput. Vis. Image Underst.*, vol. 158, pp. 1–16, 2017. 7
- [78] R. Bommasani, D. A. Hudson, E. Adeli, R. Altman, S. Arora, S. von Arx, M. S. Bernstein, J. Bohg, A. Bosselut, E. Brunskill *et al.*, “On the opportunities and risks of foundation models,” *arXiv*, 2021. 8
- [79] X. Wang, L. Xie, C. Dong, and Y. Shan, “Real-esrgan: Training real-world blind super-resolution with pure synthetic data,” in *CVPR*, 2021. 11
- [80] B. Xia, Y. Zhang, Y. Wang, Y. Tian, W. Yang, R. Timofte, and L. Van Gool, “Knowledge distillation based degradation estimation for blind super-resolution,” in *ICLR*, 2023. 11

VIII. BIOGRAPHY SECTION



Tomoki Yoshida received the bachelor and master degrees in engineering from Toyota Technological Institute in 2019 and 2021, respectively. His research interests include single-image super-resolution and its enhancement for perceptual quality improvement and blind super-resolution. His award includes the winner award in NTIRE 2018 challenge.



Yuki Kondo received the bachelor degree in engineering from Toyota Technological Institute in 2022. Currently, he is a researcher at Toyota Technological Institute. His research interests include low-level vision including image and video super-resolution and its application to tiny image analysis such as crack detection. His award includes the best practical paper award in MVA2021.



Takahiro Maeda received the bachelor and master degrees in engineering from Toyota Technological Institute in 2019 and 2021, respectively. His research interests include low-level vision and human motion tracking, synthesis, and prediction. His awards include the best poster award in MVA2019 and the first place in Real Robot Challenge 2020, the Max Planck Institute for Intelligent Systems.



Kazutoshi Akita received the bachelor and master degrees in engineering from Toyota Technological Institute in 2019 and 2021, respectively. His research interests include low-level vision including image and video super-resolution and its application to scale-free object detection. His awards include the winner award in NTIRE 2018 challenge on image super-resolution and 1st place in PIRM 2018 perceptual SR challenge.



Norimichi Ukita received the B.E. and M.E. degrees in information engineering from Okayama University, Japan, in 1996 and 1998, respectively, and the Ph.D. degree in Informatics from Kyoto University, Japan, in 2001. From 2001 to 2016, he was an assistant professor (2001 to 2007) and an associate professor (2007-2016) with the graduate school of information science, Nara Institute of Science and Technology, Japan. In 2016, he became a professor at Toyota Technological Institute, Japan. He was a research scientist of Precursory Research for Embryonic Science and Technology, Japan Science and Technology Agency, during 2002–2006, and a visiting research scientist at Carnegie Mellon University during 2007–2009. Currently, he is also an adjunct professor at Toyota Technological Institute at Chicago. Prof. Ukita’s awards include the excellent paper award of IEICE (1999), the winner award in NTIRE 2018 challenge on image super-resolution, 1st place in PIRM 2018 perceptual SR challenge, the best poster award in MVA2019, and the best practical paper award in MVA2021.